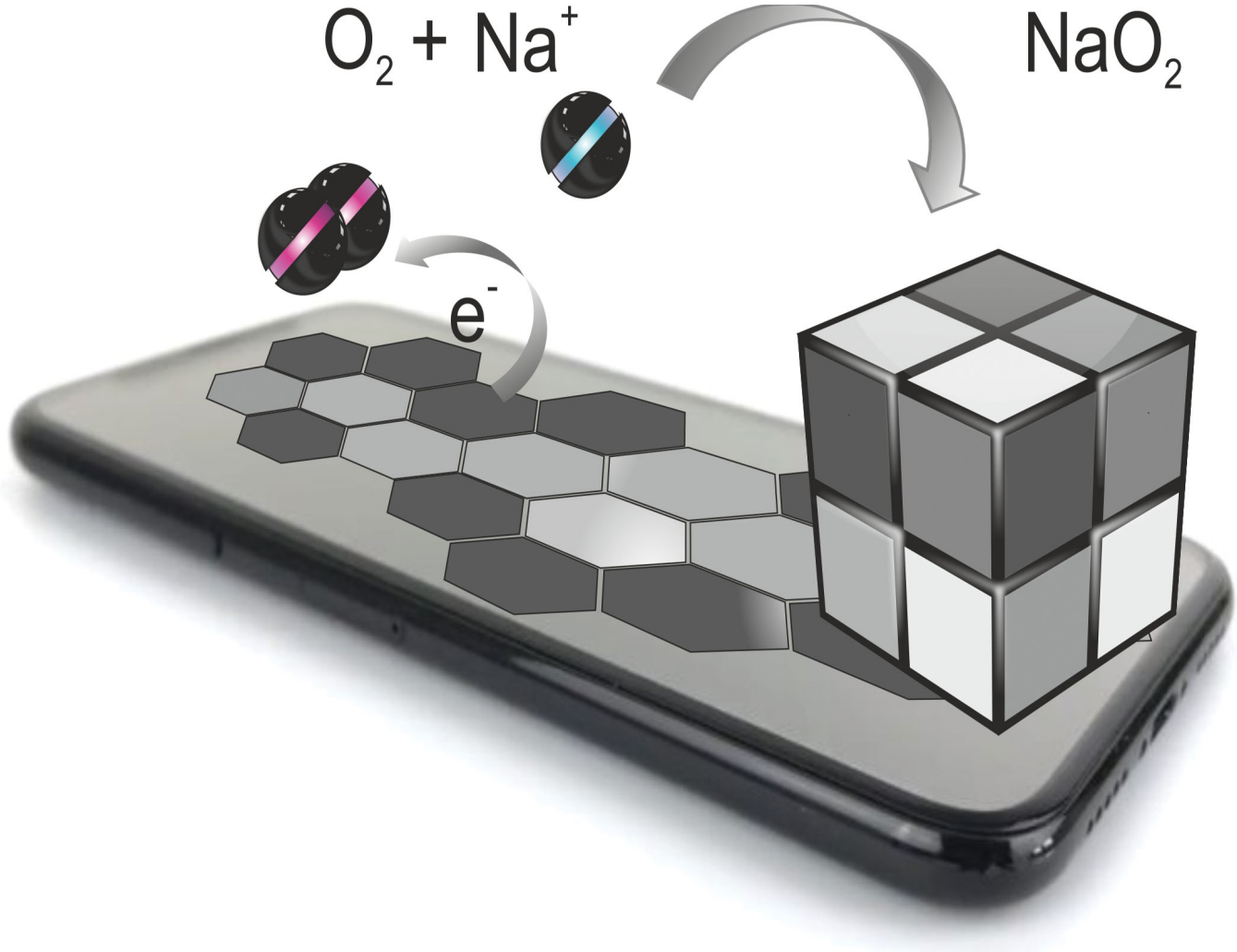

Featuring work from the research group of Professor Laurence Hardwick, University of Liverpool, UK.

Growth and dissolution of NaO_2 in an ether-based electrolyte as the discharge product in the Na–O_2 cell

The discharge product of the sodium oxygen battery is sodium superoxide (NaO_2) in the majority of electrolytes. Presented is our AFM analysis of the stages of growth of the NaO_2 revealing Rubik's cube like mesocrystal deposits.

As featured in:

See Iain M. Aldous and Laurence J. Hardwick, *Chem. Commun.*, 2018, **54**, 3444.

ROYAL SOCIETY OF CHEMISTRY

rsc.li/chemcomm

Registered charity number: 207890

ChemComm

COMMUNICATION

View Article Online
View Journal | View Issue

Cite this: *Chem. Commun.*, 2018, **54**, 3444

Received 24th October 2017,
Accepted 12th February 2018

DOI: 10.1039/c7cc08201k

rsc.li/chemcomm

Growth and dissolution of NaO_2 in an ether-based electrolyte as the discharge product in the Na–O_2 cell†

Iain M. Aldous and Laurence J. Hardwick *

The deposition and dissolution of sodium superoxide (NaO_2) was investigated by atomic force microscopy. Rectangular prisms consisting of 8 smaller sub-structures grew from NaO_2 platelets, when discharged in 0.5 M $NaClO_4$, diethylene glycol dimethyl ether on highly ordered pyrolytic graphite. During oxidation the 8 sub-structures are conserved. Ring-like structures of Na_2CO_3 of 200 nm diameter remain at the end of oxidation.

Sodium–oxygen (Na–O_2) batteries are under investigation due to the advantageous theoretical specific energy of 1106 Wh kg^{-1} for the reaction (eqn (1)):[1]

$$Na^+ + e^- + O_2 \rightarrow NaO_2 \quad E^\circ = 2.27\ V\ vs.\ Na^+/Na \qquad (1)$$

The reduction of dissolved O_2 in the presence of Na^+ results in the precipitation of large micrometre-sized cubes (1–50 μm)[2,3] of NaO_2 on the surface of the electrode. Understanding the growth and dissolution mechanism of NaO_2 cubes formed by the one-electron reduction of O_2 is critical towards the realisation of Na–O_2 as a practical technology. NaO_2 cubes are often of uniform size; however, their morphology changes based on the rate of formation. At high rates (>600 μA cm^{-2})[2] icosahedral features are formed on the electrode surface.[2] At lower rates (<400 μA cm^{-2})[2] they precipitate out as cubes.[4] The explanation of these observations is that at higher rates the amount of soluble NaO_2 formed rapidly saturates the electrolyte near the electrode interface and precipitates out as smaller cubes at many nucleation points.[2] Whereas the slower formation and saturation of the electrolyte at lower rates results in larger cubes at a decreased amount of nucleation points. Subsequently, the reaction is halted by the formation of compact insulating NaO_2 films.[5,6]

Recent reports on the growth mechanism of NaO_2 suggest that the soluble NaO_2 formed, aided by HO_2[7] catalysed intermediates, agglomerate within the solution to form cubic structures.[7] The sudden death of the cell chemistry is attributed to the formation of a passivation film between the cubic structures at the end of the discharge process, where the thickness is discharge rate dependent.[8]

Although many factors based on NaO_2 growth and morphology have been reported including rate,[2,8,9] impurity concentration,[7,10] and solvent dependence,[11–18] a unified model of the fundamental control parameters of the discharge process remains unclear, with different conclusions operating under similar conditions being made. Although there has been an extensive review carried out by Bender *et al.*[1] that ascertains the differences and similarities, Bi *et al.*[19] analysed the cell setup concluding that glass cell setups afford different discharge products (mainly $Na_2O_2{\cdot}2H_2O$) in comparison to stainless steel cell setups (NaO_2 only).

Atomic force microscopy (AFM) is a powerful method for the investigation of NaO_2 growth and dissolution reaction, as the size and morphology of the deposits can be directly measured with nanometer precision. This experimental approach has been already successfully undertaken in a lithium–oxygen (Li–O_2) battery system by Wen *et al.*[20] on highly ordered pyrolytic graphite (HOPG) and by Liu *et al.*[21] on Au. On HOPG, agglomerates of LiO_2 nanoparticles are collected and grow at step edges forming Li_2O_2 nanoplates.[20] On Au, due to the lack of step edges and a more uniform surface reactivity, Liu *et al.*[21] concluded that a soluble LiO_2 species was initially formed that subsequently precipitates out on the surface as Li_2O_2.[22] S. E. Herrera *et al.*[23] studied the formation of Li_2O_2 in DMSO on HOPG using *ex situ* AFM, and herein an analogous AFM study in the Na–O_2 system of the growth and dissolution of NaO_2 precipitates on HOPG is presented.

A CV of O_2 saturated 0.5 M $NaClO_4$, diethylene glycol dimethyl ether (DEGDME) on a HOPG surface is shown in Fig. 1a. All stated potentials are *vs.* Na^+/Na. The reductive current increase begins at the thermodynamic potential of NaO_2 formation (2.33 V) where it peaks at 1.5 V.

During the reverse scan a broad peak beginning at 2.35 V, reaching a maximum at 3.06 V, signals the electrooxidation of

Stephenson Institute for Renewable Energy, Department of Chemistry, University of Liverpool, Liverpool, L69 7ZD, UK. E-mail: hardwick@liverpool.ac.uk

† Electronic supplementary information (ESI) available: Experimental details, line profiles from AFM images and Raman spectra of NaO_2 deposits and FTIR characterisation of residual films after oxidation. See DOI: 10.1039/c7cc08201k

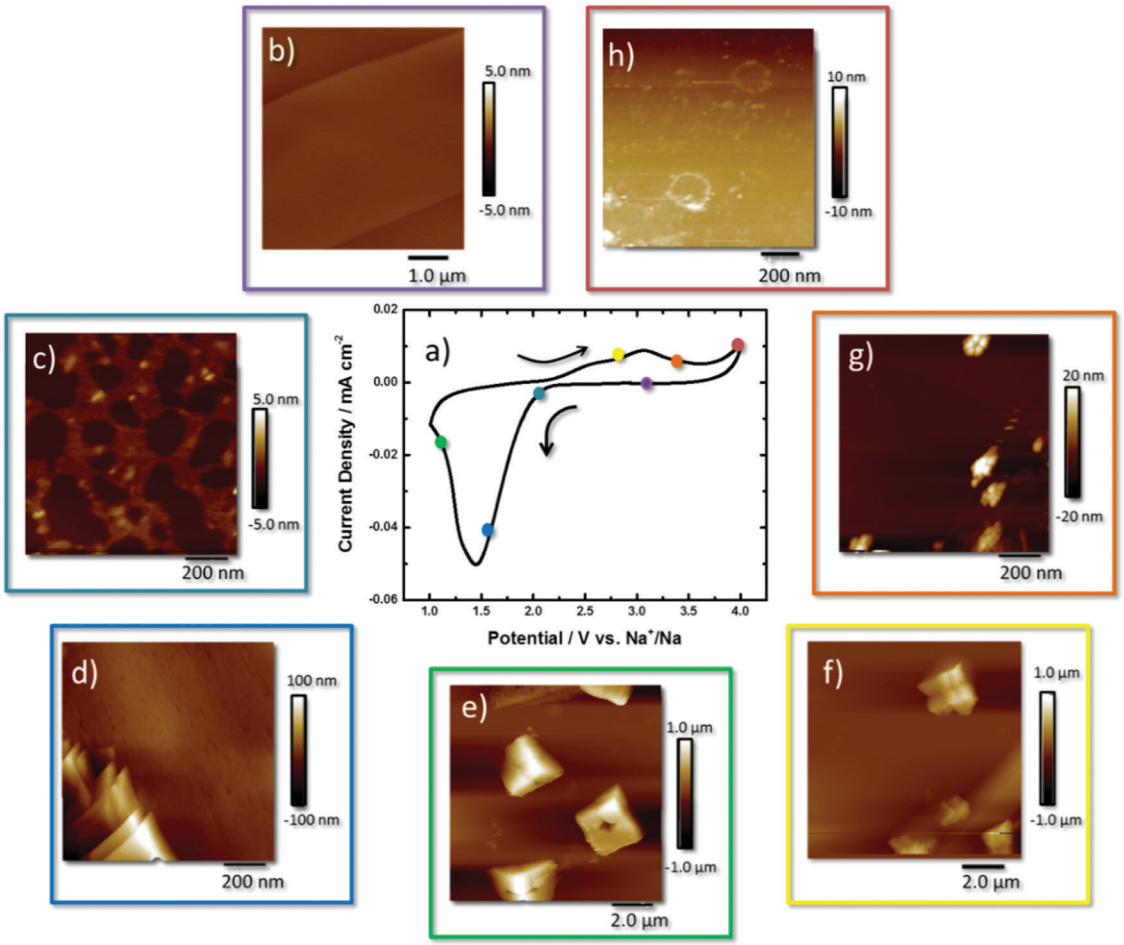

Fig. 1 (a) Cyclic voltammogram of HOPG in oxygen saturated, 0.5 M $NaClO_4$, DEGDME, AFM images taken at various potentials around the CV (b) 2.8, (c) 2.10, (d) 1.6, (e) 1.1, (f) 2.8, (g) 3.3, and (h) 4.0 V *vs.* Na^+/Na.

NaO_2 back to O_2 and Na^+. The current increases at 4.0 V, highlighting further oxidation of the remaining reaction products.[12,16,24]

The sequential description of the AFM images collected around the CV curve begins at the OCP (2.8 V) where the small striations of the freshly cleaved HOPG surface are observed that follow the step edges of the stacked graphene sheets, and the height profiles show that the step edges are 0.8 nm in height (Fig. 1b and Fig. S1, ESI†). At 2.2 V (Fig. 1c) an inhomogeneous 5 nm film of NaO_2 was observed on the surface with 20 × 20 nm sized deposits of 5 nm thickness. Calculation of the mass of the discharge product, *via* the charge passed, estimates an idealised film of 4.7 nm formed on the surface (Table S1, ESI†). Height profiles are shown in the ESI† for all measurements (Fig. S2–S7, ESI†).

The formation of 50–150 nm-thick plate-like structures of NaO_2 was observed at 1.9 V (Fig. 1d and Fig. S3, ESI†), and at 1.5 V the formation of cube-like NaO_2 crystals at the interface is observed (Fig. 1e and Fig. S4, ESI†). The NaO_2 crystals have dimensions of 2 × 2 × 1 μm, with axial lines visible on the surface along with a centralised recess that is half the deposits' height. These deposits are smaller than those observed in the literature which are generally 2–10 μm in size.[25] The Raman spectra (Fig. S8, ESI†) of these deposits show a peak at 1165 cm^{-1}, consistent with a superoxide species. The axial lines reveal a structure whereby the discrete crystal consists of stacked particles that have agglomerated on the surface and grown together. Some crystals appear prismatic or tetragonal in shape coming out of the surface, but still contain the same axial lines defining different cube-like features together, but emerging out of the plane. The depth of the hole within the centre of the crystal is ~0.5 μm in height as observed from the line profile (Fig. S4, ESI†).

Taking an extended view of the surface, the NaO_2 crystals formed at the HOPG surface are all fairly uniform in size and are both scattered across the basal plane and agglomerated along the step edge (Fig. S9, ESI†). Visible along the *x*- and *y*-axes of these features are faint lines that reveal cubic building blocks of the overall structure (Fig. 1e). The scale of the hole here suggests that the depth of this hole is in fact the height of the cube (1.0 μm). Upon closer inspection of the height profile, it is actually 0.5 μm (Fig. S4, ESI†). For other deposits, the electrode surface is visible in the middle of the cube (Fig. S10, ESI†). The secondary image taken on top of NaO_2 shows imperfect facets of the cubic structure. This is interesting as the majority of

studies show uniform NaO_2 cubes that appear as perfect plate-like structures.[26]

Upon reversing the potential back to 2.6 V, the NaO_2 are diminished in size with the axial outlines of smaller cubes making up the larger crystals still apparent (Fig. 1f and Fig. S7, ESI†). This observation concurs with the previous state where these NaO_2 crystals formed are built essentially from 8 smaller building blocks. By moving the overpotential to 3.25 V (Fig. 1g and Fig. S8, ESI†), beyond the peak current density of the redox process, very little NaO_2 is left on the HOPG surface. Only tiny agglomerates of the nanoparticles (*ca.* 20 nm in height) are observed. At 4.0 V little remains on the surface of the HOPG electrode (Fig. 1h and Fig. S9, ESI†). Nonetheless, in comparison with HOPG at the OCP (Fig. 1b), the image shows some residual material on the electrode surface, some of which form rings of *ca.* 200 nm diameter and 1.5–7 nm height, suggesting incomplete oxidation of the discharge products. This is possibly the imprints of NaO_2 deposits on the surface of the electrode (the line profile shown in Fig. S9, ESI†). The plates could be a coating of side products obtained from other reactions as indicated by Ledano *et al.*[26] and Black *et al.*[27] Only the carbon G band (1583 cm^{-1}) of HOPG is present in the Raman spectrum (Fig. S11a, ESI†). However in the FTIR spectrum, a band for Na_2CO_3 at 1429 cm^{-1} (Fig. S11b, ESI†) is detected.

Observations from the AFM study are summarised within Scheme S1 (ESI†) where initially a thin film (2–3 nm) is formed on the surface with deposits of nanoparticles of 5 nm. Platelets an order of magnitude (100 nm) higher than the film appear on the surface. On the surface as the overpotential is increased, agglomeration of cubic structures that grow into rectangular prisms of NaO_2 that consist of 8 discrete building blocks is observed. With the start of the oxidation process the edges of each crystal loses definition, leading to the presence of nano-agglomerates left at the interface. The resulting ''ghost'' shells of the crystal can be seen on the interface identified as Na_2CO_3.

Further AFM measurements (Fig. S12, ESI†) showed that NaO_2 crystallisation chemistry was found to be salt dependent and reduction of O_2 in 0.5 M NaTFSI, DEGDME in the electrolyte resulted in the formation of a holed plate-like deposit with larger dimensions of 16 × 16 × 0.5 μm. This identifies that further work needs to be undertaken to fully understand the role of the anion, as well as the ion coordination and solvent types in the electrolytes upon NaO_2 precipitation.[28]

The observation of imperfections on the NaO_2 rectangular prism including both holes and axial lines indicates the high mobility of NaO_2 particles at the interface to agglomerate and grow in discrete, potential dependent morphologies. This has implications for practical cells where controlling the type of NaO_2 precipitate will be necessary for predictable cell behaviour. The high mobility of NaO_2 indicates that agglomerates will migrate along the surface until an energy favourable site, such as a defect, is available to deposit. At the initial stage of reduction, the NaO_2 is dissolved into the electrolyte. Once the double layer is saturated with NaO_2, the deposition and formation of NaO_2 crystals can occur.

Evidence of coarsening or Ostwald ripening is found in the initial film and final stages of the reduction of O_2 (Fig. 1c) and the oxidation of NaO_2 (Fig. 1g). This is provided by the spherical nature of the particles mapped within the AFM images. These are thermodynamically more stable due to surface energy minimisation of the particles through particle dissolution and ion precipitation.[29] At this stage of formation, the precipitation of primary nanoparticles is similar to classical nanoparticle growth. Therefore at these stages of the discharge, a high concentration of monomers *i.e.* O_2^- and Na^+ should prevent particle coarsening and changes in morphology.[30,31] These effects would be heightened at an electrode interface due to the formation of the double layer structure. The anion has a considerable influence on the structure of the double layer in each system, and hence, the electrolyte anion affects these stages of NaO_2 growth, as demonstrated by the variation in deposit size between $NaClO_4$ (Fig. 1) and NaTFSI (Fig. S12, ESI†). However, classical crystallisation does not characterise the complete mechanism here due to the observation of Rubik cube-like structures.

Precursor layered plates and then Rubik cube-like structures are unsurprising given the observations of oxide formation in this solvent in the lithium analogue of this system.[20] From evidence mentioned here the steps between spherical nanoparticles of NaO_2 and rectangular prismatic structures suggest that a reoriented aggregation (RO) or mesocrystal mechanism is taking place. RO mechanisms simply encompass the aggregation of building block nanoparticles which then reorient to form single-faced structures again minimising the surface energy. Within the film the initially formed NaO_2 nanoparticles are observed (Fig. 1c). These favourable aggregation sites will then form the precipitation sites at the interface. Here collisions of aligned nanocrystals in suspension or the rotation of collided misaligned nanoparticles form the basis of growth at the interface.[31,32] Once an agglomerate of a certain size is reached, in some instances coarse ripening has been shown to smooth the edges of the final crystal structures. However, this model is not the best fit. Mesocrystal formation is a better model in this case because of the initial stages of growth proceeding into subsequent smoothing of the final precipitate. In mesocrystal formation the primary nanoparticles are iso-oriented into a crystal *via* oriented aggregation (OA).[33] Organic medium has been shown to temporarily stabilise these particles which form a mesocrystal *via* mesoscale assembly.[33] Fusion can then occur to form an oriented crystal and then finally to a single crystal. These previous observations help to explain the observations of the Rubik cube-like structures within this data series. Within this the final stage of fusion to form a single crystal is not observed (in contrast to many literature reports[33,34]), most likely due to the much shorter timescale of the voltammetry experiment and the high current rate generation of superoxide.

The process of fusion of mesocrystals, which is thermodynamically favoured under the displacement of the solvent molecules, can often include part of the organic molecule as a coating,[33] and this is proposed as a pathway for the formation of a Na_2CO_3 coating upon the formation of crystals, and a crust of Na_2CO_3 remaining on the surface of the electrode after oxidation of NaO_2.[26]

The dissolution mechanism should firstly involve the oxidation of the surface layer in contact with the surface and the edges of the

rectangular prism agglomerates. The stages characterised in this study would suggest that similar stages of dissolution are present upon dissolution as upon formation of these mesocrystals.

The scan rate used (100 mV s^{-1}) resulted in a high rate of O_2 reduction leading to initial film formation by supersaturation of the double layer providing many smaller nucleation points.[35] In the medium ionic strength electrolyte ($NaClO_4$/DEGDME), the amount of time a particle of NaO_2 can reorient itself before being fixed is lowered.[8] This observation is different from that reported by Ledrano *et al.*[6] through *in situ* electrochemical quartz mass balance measurements on Au electrodes. They concluded that there is only solution-based NaO_2 in this instance and that no film is formed until the end of the discharge. Recently Lutz *et al.*[36] have highlighted the different behaviour of this process due to the substrate, especially the difference in the observed morphology between carbon (cubic NaO_2) and Au (NaO_2 flakes) surfaces. Undoubtedly the electrode surface, solvent, salt and H_2O level have major influences on the growth and morphology of NaO_2 crystals, and further investigations are required to understand these influences.

In conclusion, *ex situ* AFM images on HOPG demonstrate the rich and intricate dissolution and recrystallisation chemistry during O_2 reduction in an aprotic ether-based solvent in the presence of Na^+. An initial formation of a 5 nm NaO_2 film followed by subsequent deposition of stacked NaO_2 platelets is observed. These plates then grow into crystalline rectangular prisms (2 × 2 × 1 μm) consisting of 8 smaller sub-structures. These were found to preferentially agglomerate at the step edges of HOPG, and also upon the basal plane itself. The observation of building block rectangular prisms that have stacked on top of each other, with striations on the deposit resembling those found on the Rubik's Cube puzzle, was unexpected, and this method of NaO_2 precipitation results in the observed 0.5 μm deep holes present in the central face of the NaO_2. Upon oxidation the dissolution of the rectangular prismatic structure conserves an unevenly shaped collection of 8 sub-structures that degrades further to groups of 40 nm-sized deposits. Rings of 200 nm diameter remain on the surface after oxidation, and these rings are thought to be the unoxidised side reaction product (Na_2CO_3) that forms on the surface of NaO_2.

Support from the Engineering and Physical Sciences Research Council grant EP/J020265/1 and the Energy SuperStore, Early Career Researcher Award is acknowledged.

Conflicts of interest

There are no conflicts to declare.

Notes and references

1 C. L. Bender, D. Schröder, R. Pinedo, P. Adelhelm and J. Janek, *Angew. Chem., Int. Ed.*, 2016, **55**, 4640–4649.
2 D. Schröder, C. L. Bender, M. Osenberg, A. Hilger, I. Manke and J. Janek, *Sci. Rep.*, 2016, **6**, 24288.
3 S. Y. Sayed, K. P. C. Yao, D. G. Kwabi, T. P. Batcho, C. V. Amanchukwu, S. Feng, C. V. Thompson and Y. Shao-Horn, *Chem. Commun.*, 2017, **53**, 460.
4 N. Ortiz-Vitoriano, T. P. Batcho, D. G. Kwabi, B. Han, N. Pour, K. P. C. Yao, C. V. Thompson and Y. Shao-Horn, *J. Phys. Chem. Lett.*, 2015, **6**, 2636–2643.
5 K. B. Knudsen, J. E. Nichols, T. Vegge, A. C. Luntz, B. D. McCloskey and J. Hjelm, *J. Phys. Chem. C*, 2016, **120**, 10799–10805.
6 I. Landa-Medrano, J. T. Frith, I. Ruiz de Larramendi, I. Lozano, N. Ortiz-Vitoriano, N. Garcia-Araez and T. Rojo, *J. Power Sources*, 2017, **345**, 237–246.
7 C. Xia, R. Black, R. Fernandes, B. Adams and L. F. Nazar, *Nat. Chem.*, 2015, **7**, 496–501.
8 J. E. Nichols and B. D. McCloskey, *J. Phys. Chem. C*, 2017, **121**, 85–96.
9 N. Zhao, C. Li and X. Guo, *Phys. Chem. Chem. Phys.*, 2014, **16**, 15646.
10 J. Kim, H. Park, B. Lee, W. M. Seong, H. D. Lim, Y. Bae, H. Kim, W. K. Kim, K. H. Ryu and K. Kang, *Nat. Commun.*, 2016, **7**, 10670–10679.
11 L. Lutz, W. Yin, A. Grimaud, D. Alves Dalla Corte, M. Tang, L. Johnson, E. Azaceta, V. Sarou-Kanian, A. J. Naylor, S. Hamad, J. A. Anta, E. Salager, R. Tena-Zaera, P. G. Bruce and J. M. Tarascon, *J. Phys. Chem. C*, 2016, **120**, 20068–20076.
12 I. M. Aldous and L. J. Hardwick, *Angew. Chem., Int. Ed.*, 2016, **55**, 8254–8257.
13 B. Wang, N. Zhao, Y. Wang, W. Zhang, W. Lu, X. Guo and J. Liu, *Phys. Chem. Chem. Phys.*, 2017, **19**, 2940–2949.
14 J. Kim, H.-D. Lim, H. Gwon and K. Kang, *Phys. Chem. Chem. Phys.*, 2013, **15**, 3623.
15 I. I. Abate, L. E. Thompson, H. C. Kim and N. B. Aetukuri, *J. Phys. Chem. Lett.*, 2016, **7**, 2164–2169.
16 B. Wang, N. Zhao, Y. Wang, W. Zhang, W. Lu, X. Guo and J. Liu, *Phys. Chem. Chem. Phys.*, 2016, **19**, 2940–2949.
17 B. Sun, K. Kretschmer, X. Xie, P. Munroe, Z. Peng and G. Wang, *Adv. Mater.*, 2017, 1606816.
18 N. Zhao and X. Guo, *J. Phys. Chem. C*, 2015, **119**, 25319–25326.
19 X. Bi, R. Wang, L. Ma, D. Zhang, K. Amine and J. Lu, *Small Methods*, 2017, **1**, 1700102.
20 R. Wen, M. Hong and H. R. Byon, *J. Am. Chem. Soc.*, 2013, **135**, 10870–10876.
21 C. Liu and S. Ye, *J. Phys. Chem. C*, 2016, **120**, 25246–25255.
22 L. Johnson, C. Li, Z. Liu, Y. Chen, S. A. Freunberger, P. C. Ashok, B. B. Praveen, K. Dholakia, J.-M. Tarascon and P. G. Bruce, *Nat. Chem.*, 2014, **6**, 1091–1099.
23 S. E. Herrera, A. Y. Tesio, R. Clarenc and E. J. Calvo, *Phys. Chem. Chem. Phys.*, 2014, **16**, 9925–9929.
24 J. Kim, H.-D. Lim, H. Gwon and K. Kang, *Phys. Chem. Chem. Phys.*, 2013, **15**, 3623–3629.
25 N. Ortiz-Vitoriano, T. P. Batcho, D. G. Kwabi, B. Han, N. Pour, K. P. C. Yao, C. V. Thompson and Y. Shao-Horn, *J. Phys. Chem. Lett.*, 2015, **6**, 2636–2643.
26 I. Landa-Medrano, A. Sorrentino, L. Stievano, I. Ruiz de Larramendi, E. Pereiro, L. Lezama, T. Rojo and D. Tonti, *Nano Energy*, 2017, **37**, 224–231.
27 R. Black, A. Shyamsunder, P. Adeli, D. Kundu, G. K. Murphy and L. F. Nazar, *ChemSusChem*, 2016, **9**, 1795–1803.
28 M. He, K. C. Lau, X. Ren, N. Xiao, W. D. McCulloch, L. A. Curtiss and Y. Wu, *Angew. Chem., Int. Ed.*, 2016, **55**, 15310–15314.
29 I. M. Lifshitz and V. V. Slyozov, *J. Phys. Chem. Solids*, 1961, **19**, 35–50.
30 X. Peng, L. Manna, W. Yang, J. Wickham, E. Scher, A. Kadavanich and A. P. Alivisatos, *Nature*, 2000, **404**, 59–61.
31 E. J. H. Lee, C. Ribeiro, E. Longo and E. R. Leite, *J. Phys. Chem. B*, 2005, **109**, 20842–20846.
32 C. Ribeiro, E. J. H. Lee, T. R. Giraldi, E. Longo, J. A. Varela and E. R. Leite, *J. Phys. Chem. B*, 2004, **108**, 15612–15617.
33 M. Niederberger and H. Cölfen, *Phys. Chem. Chem. Phys.*, 2006, **8**, 3271–3287.
34 J. Fang, B. Ding, X. Song and Y. Han, *Appl. Phys. Lett.*, 2008, **92**, 17120–17123.
35 L. C. Soare, P. Bowen, J. Lemaitre and H. Hofmann, *J. Phys. Chem. B*, 2006, **110**, 17763–17771.
36 L. Lutz, D. A. D. Corte, Y. Chen, D. Batuk, L. R. Johnson, A. Abakumov, L. Yate, E. Azaceta, P. G. Bruce, J.-M. Tarascon and A. Grimaud, *Adv. Energy Mater.*, 2017, 1701581.